Commun. Comput. Phys.
doi: 10.4208/cicp.110415.240316a

Vol. **20**, No. 5, pp. 1258-1282
November 2016

An Element Decomposition Method for the Helmholtz Equation

Gang Wang[1,2], Xiangyang Cui[1,2,*] and Guangyao Li[1,2,*]

[1] *State Key Laboratory of Advanced Design and Manufacturing for Vehicle Body, Hunan University, Changsha, 410082, P.R. China.*
[2] *Collaborative Innovation Center of Intelligent New Energy Vehicle, Shanghai, 200092, P.R. China.*

Received 11 April 2015; Accepted (in revised version) 24 March 2016

Abstract. It is well-known that the traditional full integral quadrilateral element fails to provide accurate results to the Helmholtz equation with large wave numbers due to the "pollution error" caused by the numerical dispersion. To overcome this deficiency, this paper proposed an element decomposition method (EDM) for analyzing 2D acoustic problems by using quadrilateral element. In the present EDM, the quadrilateral element is first subdivided into four sub-triangles, and the local acoustic gradient in each sub-triangle is obtained using linear interpolation function. The acoustic gradient field of the whole quadrilateral is then formulated through a weighted averaging operation, which means only one integration point is adopted to construct the system matrix. To cure the numerical instability of one-point integration, a variation gradient item is complemented by variance of the local gradients. The discretized system equations are derived using the generalized Galerkin weakform. Numerical examples demonstrate that the EDM can achieves better accuracy and higher computational efficiency. Besides, as no mapping or coordinate transformation is involved, restrictions on the shape elements can be easily removed, which makes the EDM works well even for severely distorted meshes.

AMS subject classifications: 65C20, 65N30, 65N22, 68U20

Key words: Helmholtz equation, numerical methods, element decomposition method, one-point integration, quadrilateral element, dispersion error.

1 Introduction

With the increasing demands on the acoustic performance of enclosed cavities, such as the automotive passenger compartments and aircraft cabins, careful considerations are

*Corresponding author. *Email addresses:* wanggangny@163.com (G. Wang), cuixy@hnu.edu.cn (X. Y. Cui), gyli@hnu.edu.cn (G. Y. Li)

 ©2016 Global-Science Press

https://doi.org/10.4208/cicp.110415.240316a Published online by Cambridge University Press

needed in designing these sophisticated products. The vibration noise is essentially a wave propagation phenomenon governed by the Helmholtz equation, and a large amount of research work can be found in the literature reviews [1,2].

As the analytical solution is only available for problems with very simple configurations, numerical methods for solving Helmholtz problems are becoming more and more prevalent. Over the past several decades, many efficient algorithms such as the finite element method (FEM) [3,4], the boundary element method (BEM) [5,6], the wave based method (WBM) [7], the modified smoothed particle hydrodynamics (MSPH) method [8], the hybrid-Trefftz method [9], the smoothed finite element method (SFEM) [10, 11] and the weak Galerkin (WG) method [12], etc., have already been proposed by researchers to simulate the acoustic scattering. Among these different methodologies, the standard FEM is still so far the most well-developed and widely-used numerical tool in predicting the acoustic scattering. Quadrilateral isoparametric element, which is a primary element of FEM, plays a very important role in noise simulation. However, a well-known deficiency associated with the use of quadrilateral element for the Helmholtz equation is the loss of ellipticity as the wave number increases [13], which will inevitably leads to the "pollution error". At higher frequencies, the dispersion error tends to accumulate, resulting in completely erroneous results. Although the use of more elements per wavelength can improve the numerical accuracy in acoustic analysis, the sufficiently refined mesh will leads to a dramatic increase of computational cost, especially for large scale practical acoustic problems. The accuracy of traditional quadrilateral element is also significantly depends on the mesh quality. As pointed in [14], a severely distorted mesh will cause a larger "pollution error". Since isoparametric coordinate transformation is involved in formulating the system equations, violent distorted meshes are not permitted. The third shortcoming inherent in the conventional quadrilateral element is that it suffers from a low computational efficiency. This is because four integration points are adopted when performing the numerical integration, which inevitably increase the computational cost.

Studies have found that the pollution error for one-dimensional problems can be completely eliminated by resorting to analytical solutions [15]. While for higher dimensions, the numerical dispersion cannot be completely avoided [16], but can be reduced. Over the past decades, numerous approaches to alleviating the dispersion error have been proposed by researchers, such as the Galerkin/least-squares (GLS) and Galerkin-gradient/least-square (GGLS) methods [13,17,18], the residual-free bubbles approach (RFB) [19], the multiscale finite element method (MFEM) [20], the discontinuous enrichment method (DEM) [21, 22], the weighted-averaging finite-element method (WA-FEM) [23], the modified integration rules (MIR) method [24], the discontinuous Galerkin method (DGM) [25,26], the partition of unity method (PUM) [27,28], the hybrid-Trefftz quadrilateral finite element model [9] and the finite element-least square point interpolation method (FE-LSPIM) [29, 30]. All these approaches are very promising in controlling the pollution error, and improved the numerical accuracy compared to the conventional quadrilateral element. However, the dispersion error in general two- and three-dimensional acoustic problems still cannot be eliminated properly with these al-

https://doi.org/10.4208/cicp.110415.240316a Published online by Cambridge University Press

gorithms. Besides, most of them are sensitive to mesh distortion, reasonable results can hardly obtained when severely distorted meshes are employed. Another approach in curing the inherent shortcomings of quadrilateral element is the development of meshfree methods. As no meshes are used in numerical integration, the deficiency related to element distortion encountered by mesh-based FEM can be successfully removed. Based on the meshfree methods, scholars successfully extended the element-free Galerkin method (EFGM) [31] and the radial point interpolation method (RPIM) [32] to acoustic analysis. However, the meshfree methods suffer from the low computational efficiency defect, which prevent its further application in practical engineering problems.

Recently, Cui et al. [33] proposed an element decomposition method (EDM) for analyzing two-dimensional solid mechanics problems. This element possesses a higher computational efficiency compared to the traditional full integral quadrilateral element. Besides, as no mapping or coordinate transformation is involved in formulating the system equilibrium equations, the EDM is immune to mesh distortion. Considering the superior performance of the EDM for solid mechanics problems, we further extend the EDM for acoustic analysis and expect it could cure the inherent deficiencies of quadrilateral element in this paper. Four-node quadrilateral elements, which can be generated automatically using any preprocessing software, are first used to discrete the problem domain. Then the quadrilateral element is further subdivided into four sub-triangles by directly connecting the field nodes to the centroid of the element. In each sub-triangle, the local acoustic pressure field is constructed by linear shape functions same as the practice of standard FEM, thus a constant acoustic gradient field can be expected. Based on these local acoustic quantities, the acoustic gradient field in the whole quadrilateral element is finally formed through a weighted averaging operation, which means only one integration point is adopted to construct the system matrix. In order to improve the accuracy and cure the temporal instability, a stabilization item of the stiffness matrix is complemented by variance the local gradients. Numerical examples demonstrate that the EDM possesses better accuracy and faster convergence rate without increasing the computational cost, especially for high wave number problems and severely distorted meshes.

The remainder of this paper is organized as follows. Section 2 briefly describes the theoretical basis. Section 3 introduces the detailed formulation of EDM for acoustic problems. The discretization error is outlined in Section 4. In Section 5, we assess the performance of the EDM through some numerical examples. The paper is summarized in Section 6 with some concluding remarks.

2 Mathematical model of acoustic problems

Consider an acoustic problem domain Ω bounded by Γ, provided that the acoustic field is homogeneous, inviscid and only undergoes small translational movement, the field variable p' (acoustic pressure) can then be governed by the following equation

https://doi.org/10.4208/cicp.110415.240316a Published online by Cambridge University Press

$$\Delta p' - \frac{1}{c^2}\frac{\partial^2 p'}{\partial t^2} = 0 \quad \text{in } \Omega, \tag{2.1}$$

where Δ denotes the Laplace operator, c and t are the speed of sound traveling in the fluid and time, respectively. Assuming that the acoustic pressure is a small harmonic perturbation around the steady state which satisfies

$$p' = pe^{j\omega t} \tag{2.2}$$

in which $j=\sqrt{-1}$, ω denotes the angular frequency, p is the amplitude of the acoustic pressure. Substituting Eq. (2.2) into Eq. (2.1) yields the following Helmholtz equation

$$\Delta p + \kappa^2 p = 0, \tag{2.3}$$

where κ is the wave number.

The gradient of acoustic pressure p is linked to the velocity v by the equation of motion, which gives

$$\nabla p + j\rho\omega v = 0 \tag{2.4}$$

in which ∇ denotes the gradient operator.

For interior acoustic problems studied in this work, the possible boundary conditions can be split into three parts, namely $\Gamma = \Gamma_D \cup \Gamma_N \cup \Gamma_A$. The Dirichlet, Neumann and Robin boundary conditions on Γ_D, Γ_N and Γ_A can be described as

$$\begin{aligned} &p = p_D && \text{on } \Gamma_D, \\ &\nabla p \cdot n = -j\rho\omega v_n && \text{on } \Gamma_N, \\ &\nabla p \cdot n = -j\rho\omega A_n p && \text{on } \Gamma_A, \end{aligned} \tag{2.5}$$

where v_n, A_n and ρ are, respectively, the normal velocity on the boundary Γ_N, the admittance coefficient on the boundary Γ_A and the density of medium.

3 Formulation of the EDM

3.1 The element decomposition operation

As described in Section 1, the problem domain Ω is first discretized into N_e 4-node quadrilateral elements, such that $\Omega = \Omega_1 \cup \Omega_2 \cup \cdots \cup \Omega_{Ne}$ and $\Omega_i \cap \Omega_j = \emptyset$ ($i \neq j$, $i,j = 1,2,\cdots,N_e$). For convenient, a quadrilateral element is termed as "parent" element. In the EDM, each parent element is subdivided into four sub-triangles by connecting the centroid of the element to four field nodes, and the acoustic pressure at the centroid is assumed to be the simple average of four acoustic pressures of field nodes. In each sub-triangle, the constant strain triangle element is used to compute the gradient of acoustic pressure. Then the strain smoothing technique on whole of the parent element is used to smooth the

https://doi.org/10.4208/cicp.110415.240316a Published online by Cambridge University Press

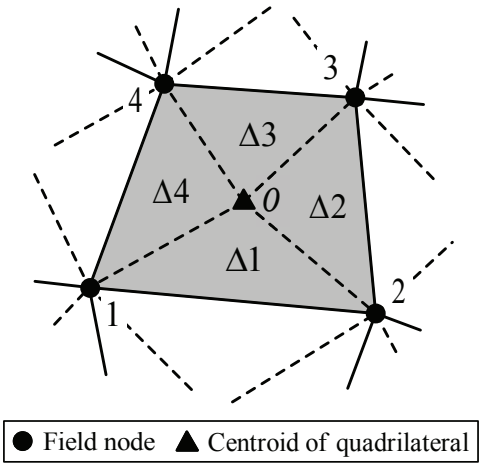


Figure 1: Division of a "parent" element into four sub-triangles.

gradients on these four sub-triangles. The formulation of EDM is presented in detail as follows.

Consider a typical quadrilateral element Ω_e as shown in Fig. 1. We first divide the element into four sub-triangles Δ_1, Δ_2, Δ_3 and Δ_4 by simply connecting the centroid O of the parent element with four field nodes.

The coordinates $\mathbf{x}_O=(x_o,y_o)^T$ of the centroid O are calculated by

$$x_O=\frac{1}{4}(x_1+x_2+x_3+x_4);\qquad y_O=\frac{1}{4}(y_1+y_2+y_3+y_4), \tag{3.1}$$

where $\mathbf{x}_i=(x_i,y_i)^{\mathrm{T}}$ $(i=1,2,3,4)$ are coordinates of four field nodes, respectively.

In the EDM, we assume the acoustic pressure p_{eO} at the centroid O is the simple average of four acoustic pressures p_{e1}, p_{e2}, p_{e3} and p_{e4} of four field nodes

$$p_{eO}=\frac{1}{4}(p_{e1}+p_{e2}+p_{e3}+p_{e4}). \tag{3.2}$$

On the first sub-triangle Δ_1, the acoustic pressure field is approximated using linear interpolation function

$$p_e^{\Delta_1}=N_1^{\Delta_1}(\mathbf{x})p_{e1}+N_2^{\Delta_1}(\mathbf{x})p_{e2}+N_3^{\Delta_1}(\mathbf{x})p_{eO} \tag{3.3}$$

in which $N_i^{\Delta_1}(\mathbf{x})$ is the shape function value for node i given by

$$\begin{aligned} &N_i^{\Delta_1}(\mathbf{x})=a_i+b_ix+c_iy\\ &a_i=\frac{1}{2A_e^{\Delta_1}}(x_jy_k-x_ky_j),\qquad b_i=\frac{1}{2A_e^{\Delta_1}}(y_j-y_k),\qquad c_i=\frac{1}{2A_e^{\Delta_1}}(-x_j+x_k), \end{aligned} \tag{3.4}$$

https://doi.org/10.4208/cicp.110415.240316a Published online by Cambridge University Press

where $A_e^{\Delta_1}$ denotes the area of the sub-triangle Δ_1, the subscript i varies from 1-2-O, j and k are determined by the cyclic permutation in the order of i, j, k.

With the relationship between the gradient of acoustic pressure and velocity presented in Eq. (2.4), the local particle velocity $\mathbf{v}_e^{\Delta_1}$ in sub-triangular cell Δ_1 can now be obtained in terms of the acoustic pressure

$$\mathbf{v}_e^{\Delta_1} = -\frac{1}{j\rho\omega}\nabla p_e^{\Delta_1} = -\frac{1}{j\rho\omega}\begin{bmatrix} \mathbf{B}_{e1}^{\Delta_1} & \mathbf{B}_{e2}^{\Delta_1} & \mathbf{B}_{e3}^{\Delta_1} \end{bmatrix}\begin{Bmatrix} p_{e1} \\ p_{e1} \\ p_{eO} \end{Bmatrix} \tag{3.5}$$

in which, the sub-matrices $\mathbf{B}_{e1}^{\Delta_1}$, $\mathbf{B}_{e2}^{\Delta_1}$ and $\mathbf{B}_{e3}^{\Delta_1}$ are given by

$$\mathbf{B}_{e1}^{\Delta_1} = \begin{bmatrix} b_1 & c_1 \end{bmatrix}^{\mathrm{T}}, \qquad \mathbf{B}_{e2}^{\Delta_1} = \begin{bmatrix} b_2 & c_2 \end{bmatrix}^{\mathrm{T}}, \qquad \mathbf{B}_{e3}^{\Delta_1} = \begin{bmatrix} b_3 & c_3 \end{bmatrix}^{\mathrm{T}}. \tag{3.6}$$

Substituting p_{eO} in Eq. (3.2) into Eq. (3.5), and then rearranging we obtain

$$\mathbf{v}_e^{\Delta_1} = -\frac{1}{j\rho\omega}\underbrace{\begin{bmatrix} \mathbf{B}_{e1}^{\Delta_1}+\frac{1}{4}\mathbf{B}_{e3}^{\Delta_1} & \mathbf{B}_{e2}^{\Delta_1}+\frac{1}{4}\mathbf{B}_{e3}^{\Delta_1} & \frac{1}{4}\mathbf{B}_{e3}^{\Delta_1} & \frac{1}{4}\mathbf{B}_{e3}^{\Delta_1} \end{bmatrix}}_{\mathbf{B}_e^{\Delta_1}}\begin{Bmatrix} p_{e1} \\ p_{e2} \\ p_{e3} \\ p_{e4} \end{Bmatrix} = -\frac{1}{j\rho\omega}\mathbf{B}_e^{\Delta_1}\mathbf{p}_e. \tag{3.7}$$

Similarly, for the second sub-triangle (triangle 2-3-O), third sub-triangle (triangle 3-4-O) and forth sub-triangle (triangle 4-1-O), the local particle velocity $\mathbf{v}_e^{\Delta_j}$ $(j=2,3,4)$ can be easily obtained through the cyclic permutation rule, which gives

$$\mathbf{v}_e^{\Delta_2} = -\frac{1}{j\rho\omega}\underbrace{\begin{bmatrix} \frac{1}{4}\mathbf{B}_{e3}^{\Delta_2} & \mathbf{B}_{e1}^{\Delta_2}+\frac{1}{4}\mathbf{B}_{e3}^{\Delta_2} & \mathbf{B}_{e2}^{\Delta_2}+\frac{1}{4}\mathbf{B}_{e3}^{\Delta_2} & \frac{1}{4}\mathbf{B}_{e3}^{\Delta_2} \end{bmatrix}}_{\mathbf{B}_e^{\Delta_2}}\begin{Bmatrix} p_{e1} \\ p_{e2} \\ p_{e3} \\ p_{e4} \end{Bmatrix} = -\frac{1}{j\rho\omega}\mathbf{B}_e^{\Delta_2}\mathbf{p}_e, \tag{3.8}$$

$$\mathbf{v}_e^{\Delta_3} = -\frac{1}{j\rho\omega}\underbrace{\begin{bmatrix} \frac{1}{4}\mathbf{B}_{e3}^{\Delta_3} & \frac{1}{4}\mathbf{B}_{e3}^{\Delta_3} & \mathbf{B}_{e1}^{\Delta_3}+\frac{1}{4}\mathbf{B}_{e3}^{\Delta_3} & \mathbf{B}_{e2}^{\Delta_3}+\frac{1}{4}\mathbf{B}_{e3}^{\Delta_3} \end{bmatrix}}_{\mathbf{B}_e^{\Delta_3}}\begin{Bmatrix} p_{e1} \\ p_{e2} \\ p_{e3} \\ p_{e4} \end{Bmatrix} = -\frac{1}{j\rho\omega}\mathbf{B}_e^{\Delta_3}\mathbf{p}_e, \tag{3.9}$$

$$\mathbf{v}_e^{\Delta_4} = -\frac{1}{j\rho\omega}\underbrace{\begin{bmatrix} \mathbf{B}_{e2}^{\Delta_4}+\frac{1}{4}\mathbf{B}_{e3}^{\Delta_4} & \frac{1}{4}\mathbf{B}_{e3}^{\Delta_4} & \frac{1}{4}\mathbf{B}_{e3}^{\Delta_4} & \mathbf{B}_{e1}^{\Delta_4}+\frac{1}{4}\mathbf{B}_{e3}^{\Delta_4} \end{bmatrix}}_{\mathbf{B}_e^{\Delta_4}}\begin{Bmatrix} p_{e1} \\ p_{e2} \\ p_{e3} \\ p_{e4} \end{Bmatrix} = -\frac{1}{j\rho\omega}\mathbf{B}_e^{\Delta_4}\mathbf{p}_e. \tag{3.10}$$

Now applying the strain smoothing operation on the constant local velocities $\mathbf{v}_e^{\Delta_1}$, $\mathbf{v}_e^{\Delta_2}$, $\mathbf{v}_e^{\Delta_3}$ and $\mathbf{v}_e^{\Delta_4}$, the particle velocity $\bar{\mathbf{v}}_e$ at the centroid of the parent element can be written as

$$\bar{\mathbf{v}}_e = \int_{\Omega_e}\mathbf{v}_e\Phi_e(\mathbf{x})d\Omega = \sum_{i=1}^{4}\mathbf{v}_e^{\Delta_i}\int_{\Delta_i}\Phi_e(\mathbf{x})d\Omega, \tag{3.11}$$

https://doi.org/10.4208/cicp.110415.240316a Published online by Cambridge University Press

where $\Phi_e(\mathbf{x})$ is a given smoothing function satisfying the following partition of unity

$$\int_{\Omega_e} \Phi_e(\mathbf{x}) d\Omega = 1. \tag{3.12}$$

The Heaviside-type piecewise constant function is employed in this research, which gives

$$\Phi_e(\mathbf{x}) = \begin{cases} 1/A_e, & \mathbf{x} \in \Omega_e, \\ 0, & \mathbf{x} \notin \Omega_e, \end{cases} \tag{3.13}$$

in which A_e is the area of the quadrilateral element. Substituting Eq. (3.13) into Eq. (3.11), the smoothed particle velocity $\bar{\mathbf{v}}_e$ now becomes

$$\bar{\mathbf{v}}_e = \frac{1}{A_e} \sum_{i=1}^{4} A_e^{\Delta_i} \mathbf{v}_e^{\Delta_i} = -\frac{1}{j\rho\omega} \bar{\mathbf{B}}_e \mathbf{p}_e, \tag{3.14}$$

where $\bar{\mathbf{B}}_e$ is the smoothed gradient matrix given by

$$\bar{\mathbf{B}}_e = \frac{1}{A_e} \sum_{i=1}^{4} A_e^{\Delta_i} \mathbf{B}_e^{\Delta_i} \tag{3.15}$$

and the acoustic gradient at the centroid of the quadrilateral element can be finally expressed using

$$\nabla \mathbf{p} = \bar{\mathbf{B}}_e \mathbf{p}_e. \tag{3.16}$$

Based on Eq. (3.16), the acoustic stiffness matrix can be easily obtained through a simple multiplication operation. As pointed in [33], element stiffness constructed in this way possesses a higher computational efficiency and it is immune to mesh distortion. However, it is temporal instable as only one integration point is used to perform the integral operation. In order to eliminate the numerical instability and improve the accuracy of the EDM, a stabilization term is complemented by introducing a variation gradient item.

As shown in Fig. 2, the quadrilateral element is again subdivided into two non-overlapping parts: $\Delta_{s1} = \Delta_1 \cup \Delta_2$ and $\Delta_{s2} = \Delta_3 \cup \Delta_4$. The weighted velocities in these two parts can be written as

$$\mathbf{v}_e^{\Delta_{s1}} = \frac{A_e^{\Delta_1} \mathbf{v}_e^{\Delta_1} + A_e^{\Delta_2} \mathbf{v}_e^{\Delta_2}}{A_e^{\Delta_1} + A_e^{\Delta_2}}; \qquad \mathbf{v}_e^{\Delta_{s2}} = \frac{A_e^{\Delta_3} \mathbf{v}_e^{\Delta_3} + A_e^{\Delta_4} \mathbf{v}_e^{\Delta_4}}{A_e^{\Delta_3} + A_e^{\Delta_4}}. \tag{3.17}$$

The variance particle velocity used to construct the variation gradient is then defined as

$$\tilde{\mathbf{v}}_e = \frac{A_e^{\Delta_1} + A_e^{\Delta_2}}{A_e} \mathbf{v}_e^{\Delta_{s1}} - \frac{A_e^{\Delta_3} + A_e^{\Delta_4}}{A_e} \mathbf{v}_e^{\Delta_{s2}}. \tag{3.18}$$

Substituting Eqs. (3.7)-(3.10) and Eq. (3.17) into Eq. (3.18), we can finally obtain

$$\tilde{\mathbf{v}}_e^{\Delta_{s1}} = -\frac{1}{j\rho\omega} \tilde{\mathbf{B}}_e \mathbf{p}_e \tag{3.19}$$

https://doi.org/10.4208/cicp.110415.240316a Published online by Cambridge University Press

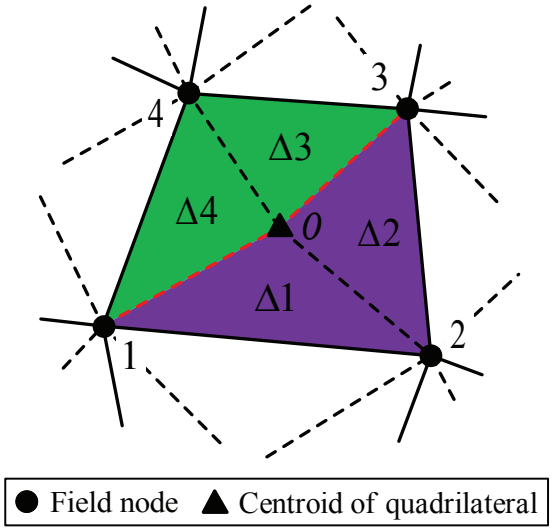


Figure 2: Division of a quadrilateral patch into two non-overlapping parts.

with the variance gradient matrix $\tilde{\mathbf{B}}_e$ given by

$$\tilde{\mathbf{B}}_e = \frac{1}{A_e}\sum_{j=1}^{2}\left(A_e^{\Delta_j}\mathbf{B}_e^{\Delta_j} - A_e^{\Delta_{j+2}}\mathbf{B}_e^{\Delta_{j+2}}\right). \tag{3.20}$$

Similar with Eq. (3.16), the variation gradient of acoustic pressure at the centroid of the parent element can now be expressed as

$$\nabla\tilde{\mathbf{p}} = \tilde{\mathbf{B}}_e\mathbf{p}_e. \tag{3.21}$$

3.2 Discretized system equations

The standard Galerkin weakform for the Helmholtz equation can be obtained by multiplying Eq. (2.3) with a test function w

$$\int_\Omega w\left(\Delta p+\kappa^2 p\right)d\Omega = 0. \tag{3.22}$$

Using Green divergence theorem and integration by parts yields

$$-\int_\Omega \nabla w\cdot\nabla p d\Omega+\kappa^2\int_\Omega w\cdot p d\Omega+\int_\Gamma w(\nabla p\cdot n)d\Gamma = 0. \tag{3.23}$$

Applying the boundary conditions presented in Eq. (2.5), we can get

$$-\int_\Omega \nabla w\cdot\nabla p d\Omega+\kappa^2\int_\Omega w\cdot p d\Omega - j\rho\omega\int_{\Gamma_N} w\cdot v_n d\Gamma - j\rho\omega\int_{\Gamma_A} w\cdot A_n p d\Gamma = 0. \tag{3.24}$$

https://doi.org/10.4208/cicp.110415.240316a Published online by Cambridge University Press

The generalized Galerkin weakform of the present element decomposition method with variance gradient item can be given by

$$-\int_\Omega \nabla w\cdot\nabla p d\Omega-\int_\Omega \nabla\tilde{w}\cdot\nabla\tilde{p}d\Omega+\kappa^2\int_\Omega w\cdot p d\Omega-j\rho\omega\int_{\Gamma_N} w\cdot v_n d\Gamma$$
$$-j\rho\omega\int_{\Gamma_A} w\cdot A_n p d\Gamma=0. \tag{3.25}$$

Substituting Eqs. (3.16) and (3.21) into Eq. (3.25), and choosing shape function as the weight function, the generalized Galerkin weakform can be rewritten as

$$\int_\Omega \bar{\mathbf{B}}^{\mathrm{T}}\bar{\mathbf{B}}\mathbf{p}d\Omega+\int_\Omega \tilde{\mathbf{B}}^{\mathrm{T}}\tilde{\mathbf{B}}\mathbf{p}d\Omega-\kappa^2\int_\Omega \mathbf{N}^{\mathrm{T}}\mathbf{N}\mathbf{p}d\Omega+j\rho\omega\int_{\Gamma_N}\mathbf{N}^{\mathrm{T}}v_n d\Gamma$$
$$+j\rho\omega\int_{\Gamma_A}\mathbf{N}^{\mathrm{T}}\mathbf{N}A_n\mathbf{p}d\Gamma=0. \tag{3.26}$$

Based on Eq. (3.26), the discretized system equations can be finally obtained and expressed in the following matrix form

$$\left[\mathbf{K}-\kappa^2\mathbf{M}+j\rho\omega\mathbf{C}\right]\{\mathbf{P}\}=-j\rho\omega\{\mathbf{F}\} \tag{3.27}$$

in which, **K** stands for the acoustic stiffness matrix assembled in the form of

$$\mathbf{K}=\sum_{e=1}^{N_e}\mathbf{K}_e=\sum_{e=1}^{N_e}\left(\bar{\mathbf{B}}_e^{\mathrm{T}}\bar{\mathbf{B}}_e A_e+\tilde{\mathbf{B}}_e^{\mathrm{T}}\tilde{\mathbf{B}}_e A_e\right). \tag{3.28}$$

M is the acoustic mass matrix defined by

$$\mathbf{M}=\sum_{e=1}^{N_e}\mathbf{M}_e=\sum_{e=1}^{N_e}\int_\Omega \mathbf{N}^{\mathrm{T}}\mathbf{N}d\Omega, \tag{3.29}$$

where the modified integration rules given in [24] will be adopted to calculate the sub-mass matrix in this research. **C** denotes the acoustic damping matrix modeling the Robin boundary condition

$$\mathbf{C}=\int_{\Gamma_A}\mathbf{N}^{\mathrm{T}}\mathbf{N}A_n d\Gamma. \tag{3.30}$$

F represents the acoustic force vector given by

$$\mathbf{F}=\int_{\Gamma_N}\mathbf{N}^{\mathrm{T}}v_n d\Gamma \tag{3.31}$$

and **P** indicates the acoustic pressure vector over the whole problem domain

$$\mathbf{P}=\{p_1,p_2,\cdots,p_n\}^{\mathrm{T}}. \tag{3.32}$$

https://doi.org/10.4208/cicp.110415.240316a Published online by Cambridge University Press

4 Numerical error in acoustic problem

For those familiar with the computational acoustics, one key issue in solving the Helmholtz equation using FEM is to control the pollution error. Studies have shown that the dispersion error is controlled by the number of points per wavelength $2\pi/\kappa h$, where h denotes the nodal spacing. This leads to the well-known "rule of the thumb" which suggests that 7 or 10 points per wavelength are needed to obtain an acceptable solution with standard finite elements. However, this criteria is not always true. In most cases, the error of numerical solutions often grows with the increase of wave number even if the criteria is satisfied.

The gradient of acoustic pressure is usually adopted as the global error indicator in numerical acoustics. Based on the relationship between the pressure and the velocity presented in Eq. (2.4), the numerical error indicator in terms of velocity can be given by

$$e_\eta^2 = \int_\Omega \left(\tilde{\mathbf{v}}^{exact} - \tilde{\mathbf{v}}^h\right)^T \left(\mathbf{v}^{exact} - \mathbf{v}^h\right) d\Omega, \tag{4.1}$$

where the superposed hat "$\sim$" denotes the complex conjugate, the superscript *exact* and h are, respectively, the exact solutions and the numerical solutions.

Ihlenburg and Babuska [34] pointed out that the error can be estimated and the relative error in H^1 semi-norm for the hp version is bounded by

$$\eta = \frac{e_\eta}{e_e} = \sqrt{\frac{\int_\Omega (\tilde{\mathbf{v}}^{exact} - \mathbf{v}^h)^T (\tilde{\mathbf{v}}^{exact} - \mathbf{v}^h) d\Omega}{\int_\Omega (\tilde{\mathbf{v}}^{exact} \cdot \mathbf{v}^{exact}) d\Omega}} \leqslant C_1 \left(\frac{\kappa h}{p}\right)^p + C_2 \kappa \left(\frac{\kappa h}{p}\right)^{2p} \tag{4.2}$$

in which C_1 and C_2 are constants that are independent to the wave number κ and mesh size h, p stands for the degree of polynomial approximation used in the numerical approaches. From Eq. (4.2), we can clearly find that the error can be split into two parts: the first one is the approximation error (the difference between the exact wave and its interpolant) and the second one is the pollution error (the difference between the interpolant and the finite element wave). For linear interpolation ($p = 1$) studied in this work, the relative error can then be rewritten as

$$\eta \leqslant C_1 \kappa h + C_2 \kappa^3 h^2. \tag{4.3}$$

5 Numerical examples

The present formulation has been coded using Matlab program. In what follows, two benchmark and one practical engineering examples are detailed studied to validate the effectiveness of the present EDM. For comparison, the QUAD4 (4-node isoparametric element integrated by 2×2 quadrature) and GLS [17] codes are also presented in this package. The CPU time is measured using the hardware platform CPU: Intel(R) Core(TM) i5-3450 (3.1 GHz); RAM 8.00 GB.

https://doi.org/10.4208/cicp.110415.240316a Published online by Cambridge University Press

5.1 2D tube with Neumann boundary condition

The first example considered here is a 2D tube filled with air as shown in Fig. 3. The geometric parameters are length $l=1.0$m and width $b=0.1$m. The left hand of the tube is subjected to a harmonic motion with normal velocity $v_n=1.0\sin\omega t$, the right hand of the tube is rigid wall and the normal velocity $v_n=0$. The density of air is 1.225kg/m^3, the speed of sound travel in the air is 340m/s. This is a widely used benchmark problem studied by many researchers, and the analytical solution is given by

$$\begin{cases} p=-j\rho_f c v_n \dfrac{\cos(\kappa(1-x))}{\sin(\kappa)}, \\ v=\dfrac{v_n \sin(\kappa(1-x))}{\sin(\kappa)}. \end{cases} \tag{5.1}$$

The problem has eigenmodes corresponding to the values

$$f=\frac{c}{2}\sqrt{\left(\frac{m}{l}\right)^2+\left(\frac{n}{b}\right)^2}, \qquad m=0,1,2,\cdots, \qquad n=0,1,2,\cdots \tag{5.2}$$

in which f are the eigenfrequencies, m and n can not be zero simultaneously.

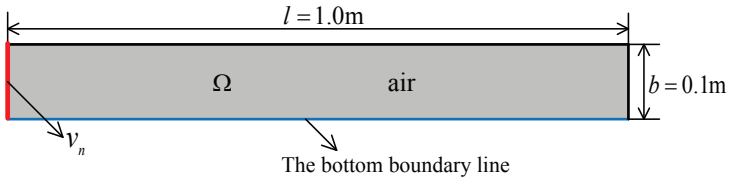


Figure 3: Model of the 2D tube.

5.1.1 Accuracy of acoustic field

The problem domain has been discretized into 160 uniformly distributed quadrilateral elements with a average nodal spacing of 25mm, as shown in Fig. 4(a). Two different wave numbers ($\kappa=15$ and $\kappa=30$) have been employed to study the performance of the present method. The numerical results of acoustic pressure along the bottom boundary line defined in Fig. 3 are plotted in Fig. 5. It can be seen from these plots that:
(1) For low wave number problems, as shown in Fig. 5(a), both the three methods can give very similar results which are in good agreement with the exact solution.
(2) With the increase of wave number, as shown in Fig. 5(b), the EDM can still provides very accurate acoustic predictions; the QUAD4, however, deviate a lot from the exact one; the performance of GLS fall in between.

In order to demonstrate the accuracy in quantity, a local relative error in acoustic pressure is defined as

$$e_p=\frac{|p^{exact}-p^h|}{p^{exact}}\times 100\%. \tag{5.3}$$

https://doi.org/10.4208/cicp.110415.240316a Published online by Cambridge University Press

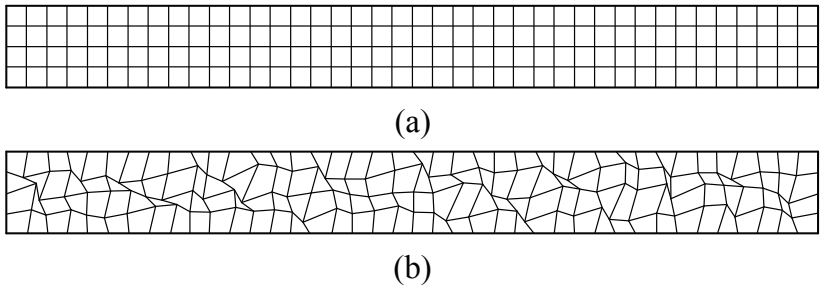


Figure 4: Two meshes for the 2D tube: (a) Regular mesh; (b) Irregular mesh.

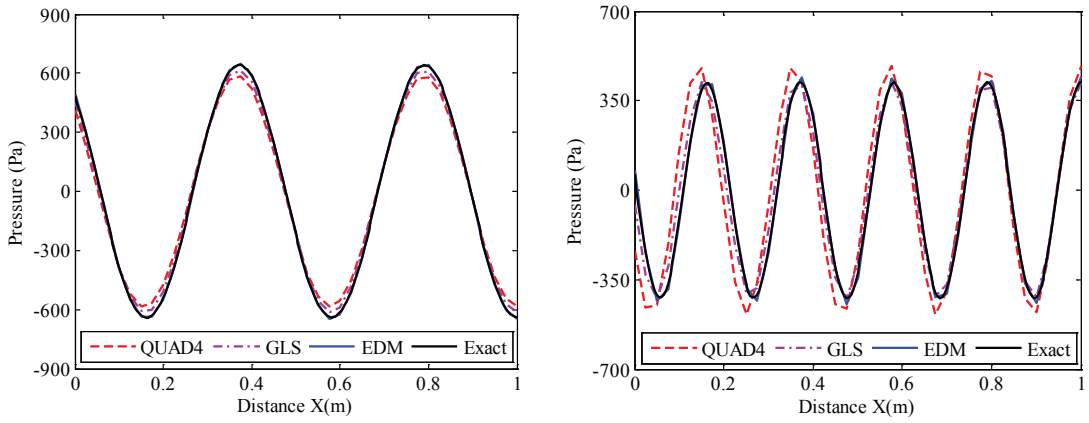


Figure 5: Numerical and exact solutions of acoustic pressure for the 2D tube (a) $\kappa=15$; (b) $\kappa=30$.

The local relative error along the bottom boundary line is depicted in Fig. 6(a), in which the wave number is prescribed to be 15. The acoustic particle velocity linked to the gradient of acoustic pressure is shown in Fig. 6(b). From these figures, we can clearly find that the peak of relative errors for the three methods both occur where the velocity is the maximum, but the local relative error of EDM is much small compared to the other two approaches. This fact again illustrates that the present EDM possesses a better accuracy in solving the acoustic problems.

5.1.2 Convergence study

The convergence properties of the present EDM, QUAD4 and GLS are investigated in this subsection. Fig. 7 plots the convergence rate in terms of the global relative error η against the average mesh size h at wave number of 15 and 30. It is easily noticed that

(1) The present EDM can achieves a faster convergence rate compared with the traditional QUAD4 and GLS.

https://doi.org/10.4208/cicp.110415.240316a Published online by Cambridge University Press

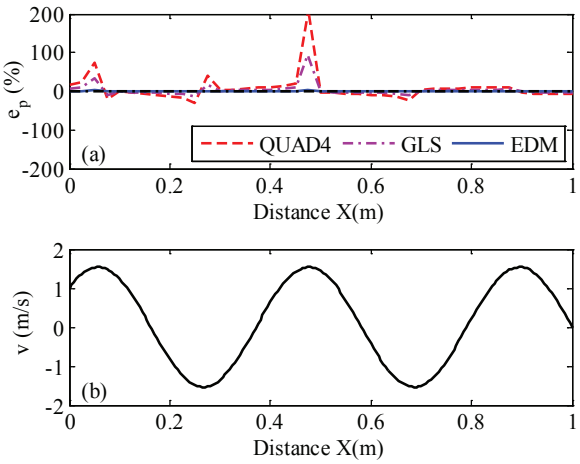


Figure 6: (a) Local relative error in acoustic pressure; (b) velocity along the bottom boundary line.

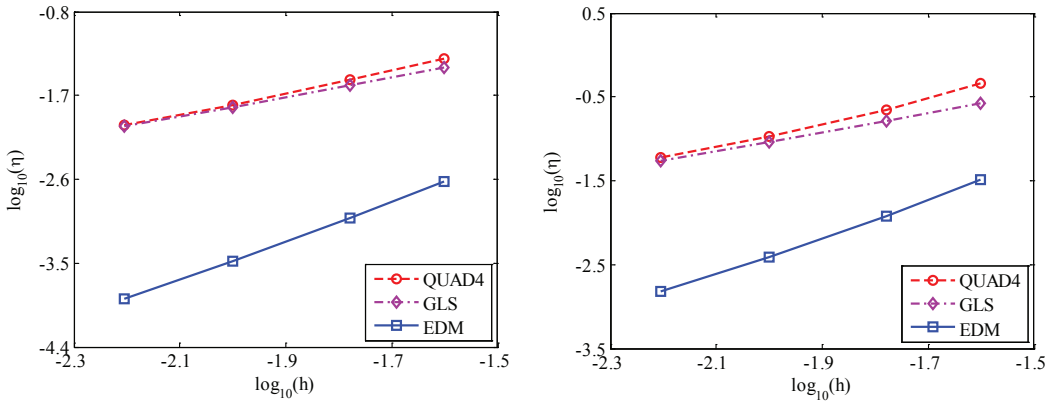


Figure 7: Comparison of accuracy and convergence property: (a) $\kappa=15$; (b) $\kappa=30$.

(2) Though the relative error grows with the increase of wave number, the EDM possesses a better accuracy among all the compared models, especially for high wave number problems.

The sensitivity of the relative error against the non-dimensional wave number is then studied with constant mesh size. Fig. 8 compares the global relative error obtained using the EDM, together with those of the QUAD4 and GLS. The interpolation error (κh) and numerical dispersion error ($\kappa^3 h^2$) are also depicted in the plot. As can be seen from the figure that:

(1) The relative errors obtained from all three numerical approaches are very small at low wave numbers.

https://doi.org/10.4208/cicp.110415.240316a Published online by Cambridge University Press

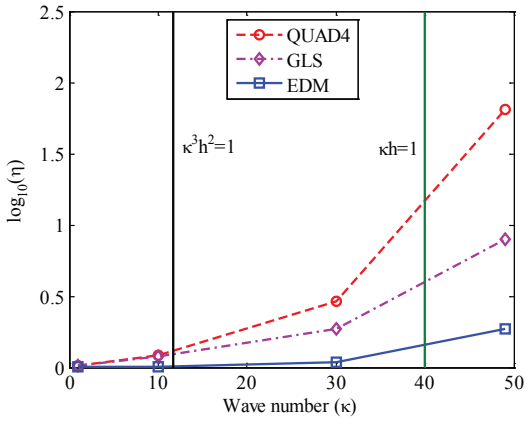


Figure 8: Relative error changing with non-dimensional wave number based on the same mesh.

(2) With the increase of wave number, the relative errors grow dramatically for both methods. However, the numerical errors obtained from the present method are much small compared to the other two approaches.

These findings further illustrate that the EDM is less sensitive to the increase of wave number and can provides very reliable acoustic pressure predictions than QUAD4 and GLS in the high frequency range.

5.1.3 Efficiency study

Now we mention the computational efficiency of the present method compared with the QUAD4 and GLS models. Both the codes are complied by a personal computer with the hardware platform given at the beginning of this chapter. The global relative error against the CPU time at the wave number of 30 are plotted in Fig. 9. It is seen that the

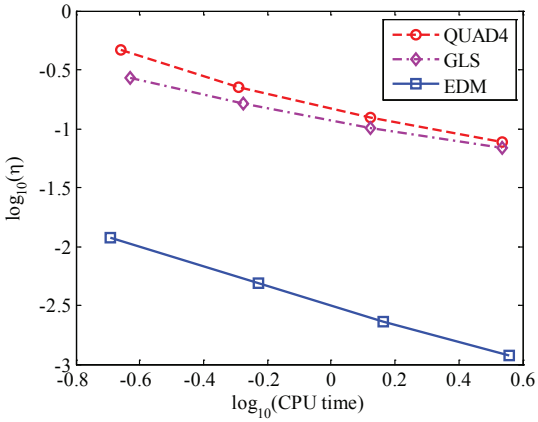


Figure 9: Relationship between the relative error and the CPU time.

https://doi.org/10.4208/cicp.110415.240316a Published online by Cambridge University Press

EDM possesses the highest computational efficiency (CPU time for the same accuracy) compared to the traditional QUAD4 and GLS. This is partly because (1) only one integration point is adopted to calculate the acoustic stiffness matrix in EDM, while the QUAD4 and GLS implement a full integration process, thus the EDM spends less CPU time compared with the other two methods; (2) the EDM possesses a higher computational accuracy.

5.1.4 Acoustic eigenfrequencies analysis

As the modal quantities, such as the eigenfrequencies and the eigenmodes, play an important role in evaluating the acoustic performance for a practical engineering product, thus such an investigation solved using EDM and standard QUAD4 is further conducted in this subsection. The tube is discretized into 160 uniformly distributed quadrilateral elements with a average nodal spacing of 25mm which satisfies the "rule of the thumb", guaranteeing a frequency limit of 2164.5Hz. The first 20 natural eigenfrequencies obtained from the EDM and QUAD4 with the same mesh are listed in Table 1. The analytical solutions are also given for comparison. As indicated in the table:

Table 1: 2D tube natural frequencies calculated using QUAD4 and EDM.

	QUAD4		EDM		
Mode order	Eigenvalue	Error (%)	Eigenvalue	Error (%)	Exact (Hz)
1	170.04	0.0257	170.00	-0.0000	170.00
2	340.35	0.1028	340.00	-0.0001	340.00
3	511.18	0.2315	510.00	-0.0006	510.00
4	682.80	0.4117	679.99	-0.0020	680.00
5	855.47	0.6437	849.96	-0.0050	850.00
6	1029.46	0.9277	1019.89	-0.0104	1020.00
7	1205.04	1.2637	1189.77	-0.0193	1190.00
8	1382.47	1.6520	1359.55	-0.0330	1360.00
9	1562.02	2.0927	1529.19	-0.0530	1530.00
10	1743.96	2.5859	1698.62	-0.0812	1700.00
11	1743.96	2.5859	1698.62	-0.0812	1700.00
12	1752.23	2.5608	1706.02	-0.1440	1708.48
13	1776.86	2.4919	1728.03	-0.3249	1733.66
14	1817.33	2.3937	1764.10	-0.6059	1774.85
15	1872.86	2.2891	1813.39	-0.9593	1830.95
16	1928.56	3.1315	1867.77	-0.1194	1870.00
17	1942.48	2.1998	1874.85	-1.3586	1900.67
18	202514	2.1498	1947.32	-1.7757	1982.52
19	2116.08	3.7295	2029.59	-0.5102	2040.00
20	2119.79	2.1532	2036.53	-1.8590	2075.11

https://doi.org/10.4208/cicp.110415.240316a Published online by Cambridge University Press

(1) for lower eigenfrequencies, the EDM can provides much more accurate numerical solutions than the QUAD4.

(2) With the increase of eigenfrequencies, the results obtained from QUAD4 deviate a lot from the analytical one, while the present method can still gives very accurate eigenfrequencies prediction.

5.1.5 Effects of nodal irregularity

In order to evaluate the sensitivity of the present method for mesh distortion, the influence of nodal irregularity on accuracy of solutions will be detailed studied in this subsection. The irregularly distributed nodes are generated by manipulating the regular nodes according to the following equation

$$\begin{aligned} x_{ir} &= x + \Delta x \cdot r_c \cdot \alpha_{ir}, \\ y_{ir} &= y + \Delta y \cdot r_c \cdot \alpha_{ir}, \end{aligned} \tag{5.4}$$

where x and y are the initial regular coordinates. x_{ir} and y_{ir} are newly irregular coordinates. Δx and Δy are the initial regular nodal spacing in the x and y directions, respectively. r_c is a computer-generated random number varying from -1.0 to 1.0. α_{ir} is a prescribed irregularity factor ranging between 0.0 and 0.5. Clearly, a bigger value of α_{ir} will lead to a severely distorted mesh. A typical irregular mesh discretization used in this study is shown in Fig. 4(b), where the irregularity factor is fixed to be 0.5.

Fig. 10 plots the acoustic pressure distribution along the bottom boundary line obtained from the present method, together with those of the QUAD4 and GLS at the wave number of 30. The global relative errors corresponding to these three methodologies are depicted in Fig. 11. It is observed that the numerical solutions derived from both QUAD4 and GLS depart a lot from the exact one, while the EDM can still provides "close-to-exact" acoustic pressure predictions. This crucial finding indicates that

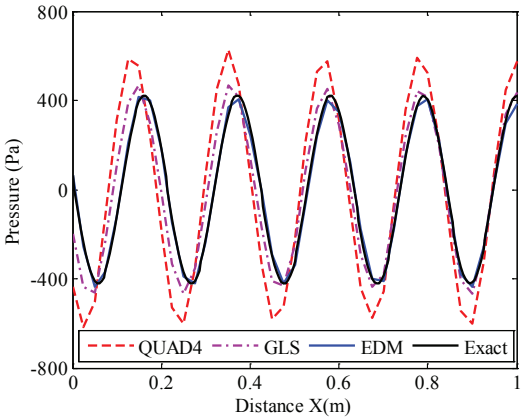


Figure 10: Effect of irregular mesh on accuracy at wave number of 30.

https://doi.org/10.4208/cicp.110415.240316a Published online by Cambridge University Press

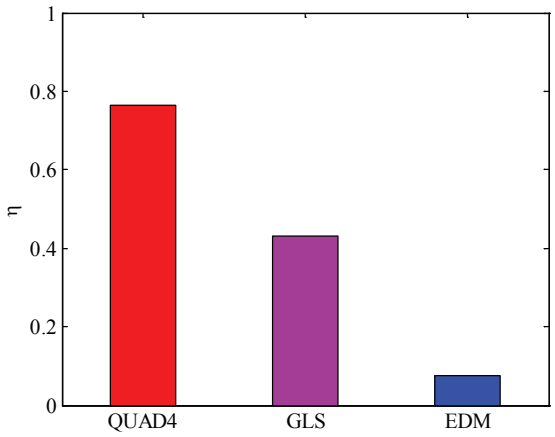


Figure 11: Comparison of the relative error at wave number of 30.

the present method works well even for extremely distorted meshes. The QUAD4 and GLS, however, are known and confirmed here being more sensitive to mesh distortions. In practical engineering problems, it is impossible to discretize the problem domain with regularly distributed meshes, which implies the present EDM has a huge project application value.

5.2 The acoustic square domain problem

As shown in Fig. 12, a square domain problem with length $L=1$m subjected to Robin boundary conditions on all four sides is further studied to illustrate the accuracy and efficiency of the present EDM. The medium parameters are same as in Subsection 5.1. This example was originally modeled by Bouillard et al. [31] and later investigated by Harari et al. [35] and Yao et al. [14]. The pressure is prescribed at one of the corners. The strong form of this problem can be expressed using the following non-dimensional Helmholtz equation

$$\frac{\partial^2 p}{\partial \xi^2}+\frac{\partial^2 p}{\partial \eta^2}+\kappa^2 p=0 \qquad \text{in } \Omega\ (0\le\xi\le 1;\ 0\le\eta\le 1) \tag{5.5}$$

with the Dirichlet boundary condition $p(0,0)=1$ and the Robin boundary conditions

$$\begin{cases} -\dfrac{\partial p}{\partial \xi}+j\kappa p\cos\beta=0 & \text{on } (\xi=0,\ \eta), \\ \dfrac{\partial p}{\partial \xi}-j\kappa p\cos\beta=0 & \text{on } (\xi=1,\ \eta), \\ -\dfrac{\partial p}{\partial \eta}+j\kappa p\sin\beta=0 & \text{on } (\xi,\ \eta=0), \\ \dfrac{\partial p}{\partial \eta}-j\kappa p\sin\beta=0 & \text{on } (\xi,\ \eta=1). \end{cases} \tag{5.6}$$

https://doi.org/10.4208/cicp.110415.240316a Published online by Cambridge University Press

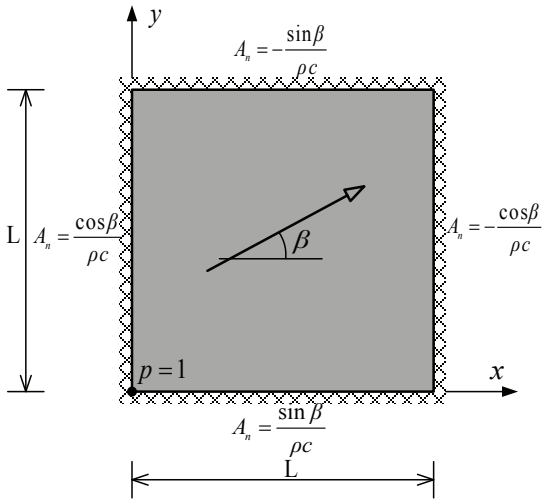


Figure 12: Plane wave in square domain: problem statement.

This two-dimensional problem corresponds to a plane wave propagating along a direction inclined with an angle β on axis x, and the analytical acoustic pressure is

$$p=\cos[\kappa(\xi\cos\beta+\eta\sin\beta)]+j\sin[\kappa(\xi\cos\beta+\eta\sin\beta)]. \tag{5.7}$$

Two different frequencies, namely $f=300$Hz and 800Hz, are employed here to study the accuracy and convergence of the present method. The inclined angle β is first assumed to be 30°. The global relative errors in the H^1 semi-norm computed using the present EDM, together with that obtained from the QUAD4 and GLS, at these two frequencies are shown in Fig. 13. The results demonstrate that (1) no matter low (300Hz) or

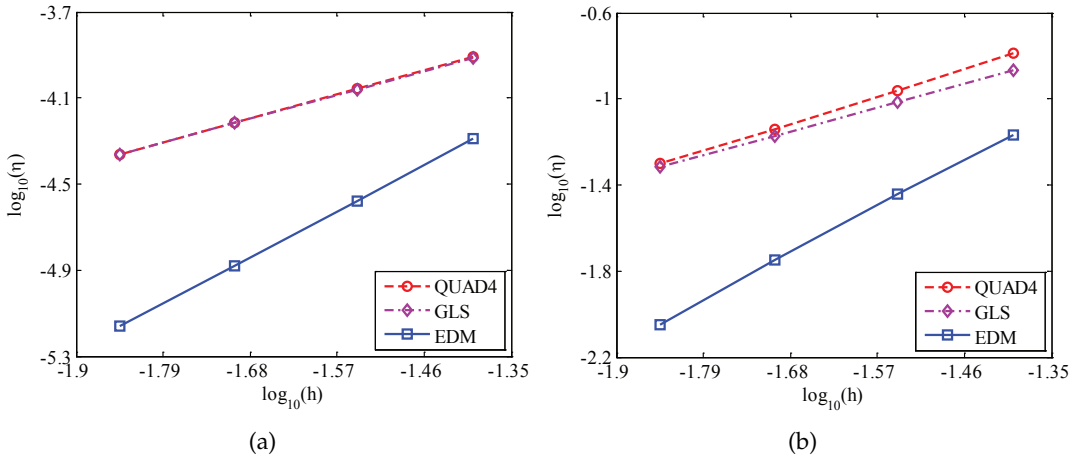


Figure 13: Comparison of accuracy and convergence when $\beta=30°$: (a) $f=300$Hz; (b) $f=800$Hz.

https://doi.org/10.4208/cicp.110415.240316a Published online by Cambridge University Press

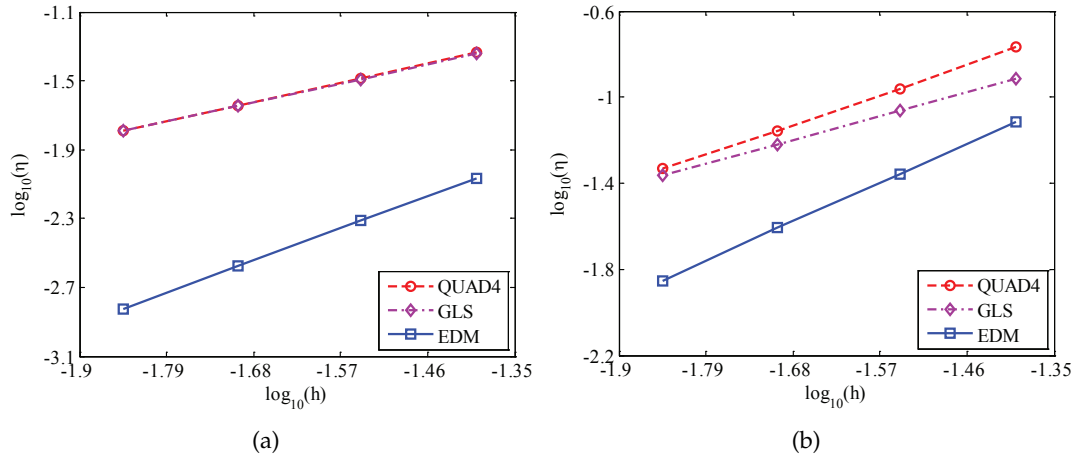


Figure 14: Comparison of accuracy and convergence when $\beta=45°$: (a) $f=300$Hz; (b) $f=800$Hz.

high (800Hz) frequency values are investigated, the EDM possesses the better accuracy and faster convergence rate among all the compared models; (2) at low frequency, the GLS has a similar accuracy and convergence rate compared to the QUAD4; however, it performs slightly better than the latter when high frequency value is tested. Similar to the problem solved in [14], the case of $\beta=45°$ is also studied in this subsection. The convergence rate in terms of the global relative error η against the average mesh size h at these two frequency values are depicted in Fig. 14(a) and 14(b), respectively. Again, the EDM performs better than the QUAD4 and GLS. These crucial findings further demonstrate the good behaviour of the EDM on 2D problems.

Then, we investigate the computational efficiency of the present EDM, compared to that of the QUAD4 and GLS. The computational cost is to set up the global stiffness and mass matrices and to solve the algebraic equations. Both the two inclined angles (30° and 45°) are employed here to implement the study. Fig. 15 illustrates the global relative error indicator (η) against the CPU time for $f=800$Hz. It is observed that the EDM possesses the highest computational efficiency compared to the other two methodologies. This finding confirms the conclusion summarized in Subsection 5.1.3. Hence, the EDM can be seen as a good candidate in solving two-dimensional acoustic problems.

5.3 Radiation in an automotive interior

During the conceptual phases of car design, the geometry of the occupant compartment can be approximately considered as prismatic and it is possible to simplify the three dimensional space to a two dimensional domain. Fig. 16(a) illustrates the 2D geometry of the problem domain with horizontal length $L_x=2.664$m and vertical length $L_y=1.121$m. The density of air is 1.225kg/m^3 and the speed of sound is 340m/s. One of the main sources generating noise in the passenger compartment is the vibration of the firewall,

https://doi.org/10.4208/cicp.110415.240316a Published online by Cambridge University Press

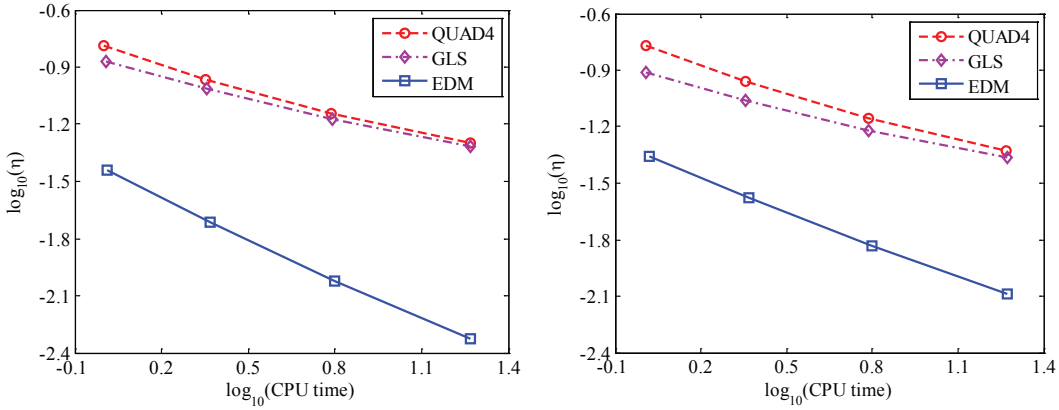


Figure 15: Relationship between the global relative error and the CPU time: (a) $\beta=30°$; (b) $\beta=45°$.

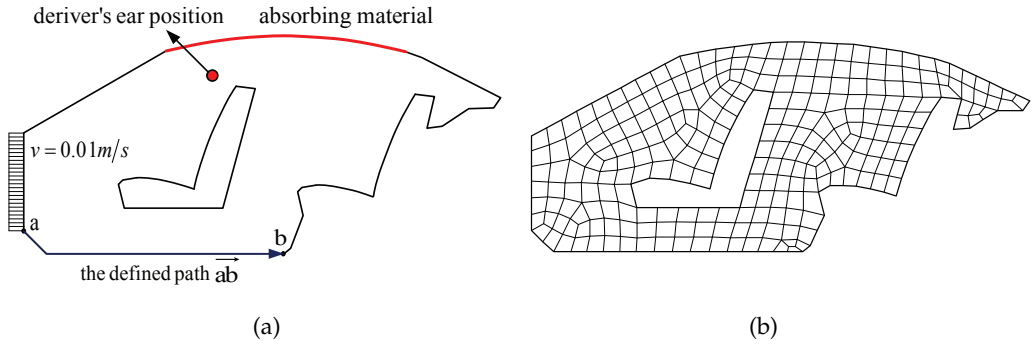


Figure 16: (a) The model of a 2D car interior cavity; (b) Mesh discretization.

which gives a Neumann boundary condition with velocity $v_n=0.01$m/s. The roof of the cabin is fixed with absorbing material with admittance $A_n=0.00144$m/(Pa·s). During the analysis, the problem domain is discretized into 257 irregularly distributed quadrilateral elements with a average nodal spacing of 0.12m, which gives a frequency limit of 451 Hz according to "rule of the thumb", as shown in Fig. 16(b).

Fig. 17(a)-(c) plot the acoustic pressure distribution in the passenger compartment at 250Hz obtained from the QUAD4, GLS and EDM, respectively. While the numerical solutions derived at 450Hz are presented in Fig. 18(a)-(c). Because the exact solution for this practical problem is unavailable, a reference configuration obtained using FEM with a very fine mesh (30775 nodes with 30180 quadrilateral elements) is adopted for comparison and the results at 250Hz and 450Hz are plotted in Figs. 17(d) and 18(d), respectively. From these figures, we can clearly find that the contours of the pressure obtained from all three approaches are similar compared with the reference solution for 250Hz. When it comes to higher frequency (450Hz), the contour of the pressure derived

https://doi.org/10.4208/cicp.110415.240316a Published online by Cambridge University Press

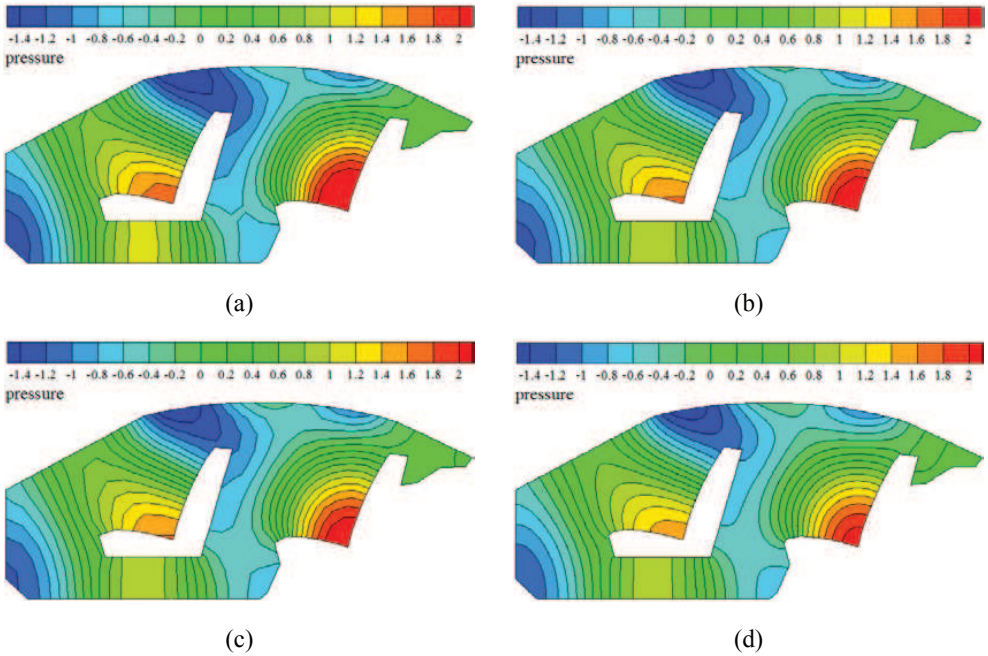


Figure 17: Real part of acoustic pressure distribution for 250 Hz: (a) QUAD4; (b) GLS; (c) EDM; (d) Reference.

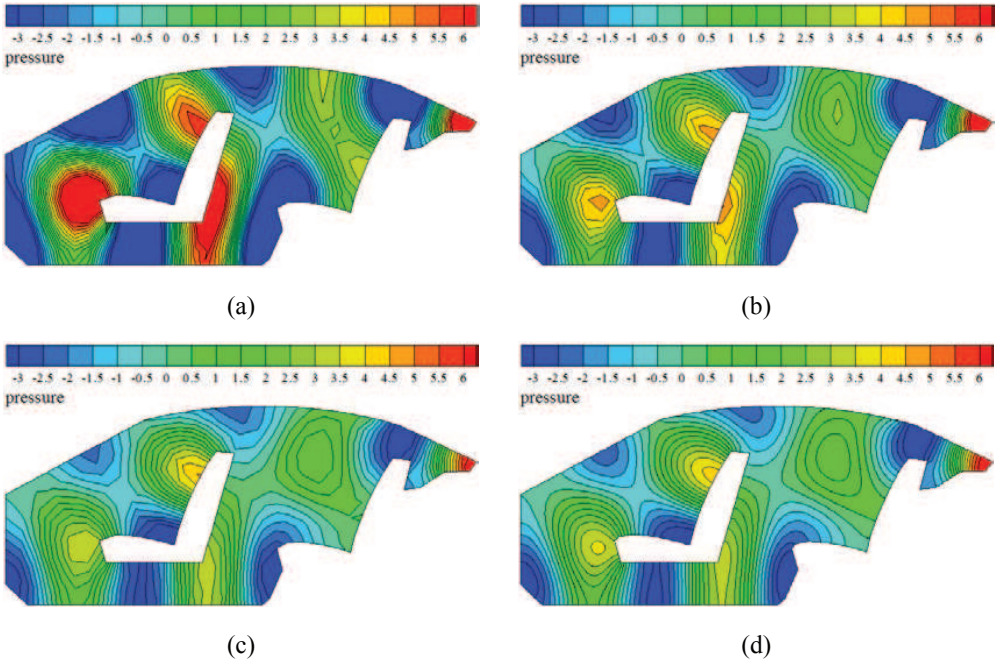


Figure 18: Real part of acoustic pressure distribution for 450 Hz: (a) QUAD4; (b) GLS; (c) EDM; (d) Reference.

https://doi.org/10.4208/cicp.110415.240316a Published online by Cambridge University Press

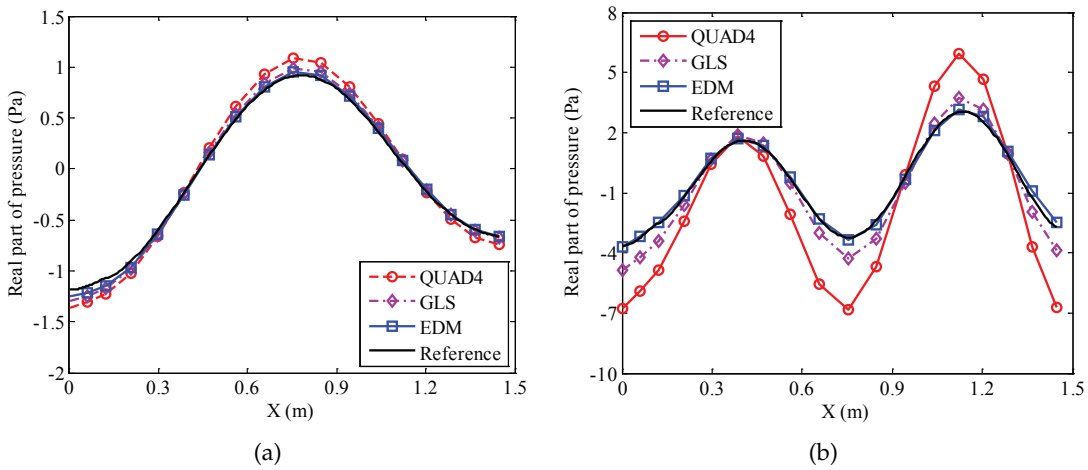


Figure 19: Real part of acoustic pressure distribution along the defined path ab: (a) 250 Hz; (b) 450 Hz.

from EDM still agrees very well with the reference one, while the QUAD4 error is obvious due to the dispersion, as most of the contours departing from the reference solution. The GLS performs better than QUAD4 but worse compared to the present EDM.

In order to depict the results quantitatively, the real part of acoustic pressure obtained using different numerical approaches along the defined path *ab* are plotted in Fig. 19(a) and (b), respectively. It is observed that (1) though the three methodologies can both give reasonable acoustic pressure predictions at lower frequency value (250Hz), the present EDM is obviously a winner among all the compared models; (2) when it comes to higher frequency (450Hz), the GLS and QUAD4 can no longer provide reliable solutions, while the numerical solution obtained from the present method still agrees very well with the reference one.

The direct frequency response analysis is then conducted based on the same mesh shown in Fig. 16(b). A full range frequency sweep is studied from 1Hz to 600Hz at intervals of 1.0Hz, which is far beyond the frequency limit of 451Hz according to "rule of the thumb". The sound pressure levels (SPL) at the driver's ear point is measured. The responses obtained using the present EDM, QUAD4 and GLS are plotted in Fig. 20. Clearly, the EDM can provides a better result compared with the other two methods in the full frequency range. At lower frequency range, both the QUAD4 and GLS solutions agree very well with the reference one. However, large deviations between these two numerical results and the reference can be found in the higher frequency range.

6 Concluding remarks

In this work, an element decomposition method (EDM) is presented for solving two-dimensional acoustic problems. Through the formulations and numerical examples, some

https://doi.org/10.4208/cicp.110415.240316a Published online by Cambridge University Press

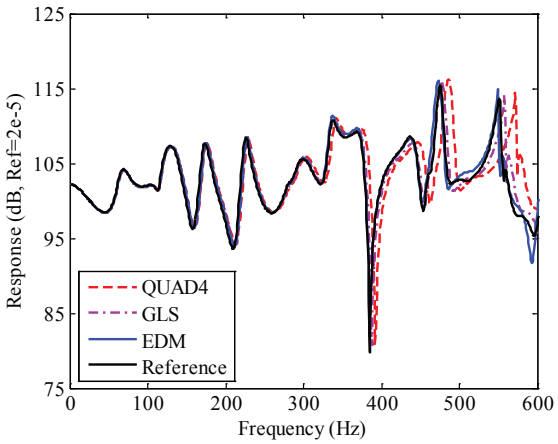


Figure 20: Acoustic frequency response at driver's ear position.

concluding remarks can be drawn as follows:

(1) As only one integration point is adopted to formulate the acoustic stiffness matrix, the present EDM can significantly reduces the computational cost compared with the conventional QUAD4 and GLS.

(2) No coordinate transformation or mapping is performed in EDM, which makes the present method less sensitive to mesh distortion. Thus the domain discretization is more flexible than traditional quadrilateral isoparametric element.

(3) The EDM possesses higher computational efficiency and faster convergence rate than the traditional QUAD4 and GLS.

(4) The present method is less sensitive to the increase of wave number and can significantly reduces the dispersion error, especially for large wave number problems.

(5) The EDM is very simple and can be easily implemented with little changes to the FEM codes.

Through the obtained results, it is indicates that the present method is thus very promising to provide a simple and effective tool for analyses of acoustic problems.

Acknowledgments

This work was supported by the National Science Foundation of China (11472101), State Key Program of National Natural Science of China (61232014), Science Fund of State Key Laboratory of Advanced Design and Manufacturing for Vehicle Body (71575003) and Hunan Provincial Natural Science Foundation of China (2015JJ3037).

https://doi.org/10.4208/cicp.110415.240316a Published online by Cambridge University Press

References

[1] L.L. Thompson, A review of finite-element methods for time-harmonic acoustics, J. Acoust. Soc. Am., 119 (2006), 1315-1330.
[2] J.T. Chen, Recent development of dual BEM in acoustic problems, Comput. Methods Appl. Mech. Engrg., 188 (2000), 833-845.
[3] F. Ihlenburg, I. Babuska, Dispersion analysis and error estimation of Galerkin finite element methods for the Helmholtz equation, Int. J. Numer. Meth. Engng., 38 (1995), 3745-3774.
[4] F. Ihlenburg, I. Babuska, Finite element solution for the Helmholtz equation with high wave number. Part I: The h-version of the FEM, Computers Math. Applic., 30 (1995), 9-37.
[5] L. Gaul, M. Wagner, W. Wenzel, N. Dumont, Numerical treatment of acoustic problems with the hybrid boundary element method, Int. J. Solids Struct., 38 (2001), 1871-1888.
[6] S. Li, Q. Huang, A new fast multipole boundary element method for two dimensional acoustic problems, Comput. Methods Appl. Mech. Engrg., 200 (2011), 1333-1340.
[7] B.V. Genechten, O. Atak, B. Bergen, E. Deckers, S. Jonckheere, J.S. Lee, A. Maressa, K. Vergote, B. Pluymers, D. Vandepitte, W. Desmet, An efficient wave based method for solving Helmholtz problems in three-dimensional bounded domains, Eng. Anal. Bound. Elem., 36 (2012), 63-75.
[8] G.M. Zhang, R.C. Batra, Wave propagation in functionally graded materials by modified smoothed particle hydrodynamics (MSPH) method, J. Comput. Phys., 222 (2007), 374-390.
[9] K.Y. Sze, G.H. Liu, H. Fan, Four- and eight-node hybrid-Trefftz quadrilateral finite element models for Helmholtz problem, Comput. Methods Appl. Mech. Engrg., 199 (2010), 598-614.
[10] W. Li, Y.B. Chai, M. Lei, G.R. Liu, Analysis of coupled structural-acoustic problems based on the smoothed finite element method (S-FEM), Eng. Anal. Bound. Elem., 42 (2014), 84-91.
[11] E. Li, Z.C. He, X. Xu, G.R. Liu, Hybrid smoothed finite element method for acoustic problems, Comput. Methods Appl. Mech. Engrg., 283 (2015), 664-688.
[12] L. Mu, J.P. Wang, X. Ye, S. Zhao, A numerical study on the weak Galerkin method for the Helmholtz equation, Commun. Comput. Phys., 15 (2014), 1461-1479.
[13] I. Harari, F. Magoules, Numerical investigation of stabilized finite element computations for acoustics, Wave Motion, 39 (2004), 339-349.
[14] L.Y. Yao, D.J. Yu, X.Y. Cui, X.G. Zang, Numerical treatment of acoustic problems with the smoothed finite element method, Appl. Acoust., 71 (2010), 743-753.
[15] F. Ihlenburg, Finite Element Analysis of Acoustic Scatting (Applied Mathematical Sciences), New York: Springer-Verlag, 1998.
[16] I. M, Babuska, S.A. Sauter, Is the pollution effect of the FEM avoidable for the Helmholtz equation considering high wave numbers?, SIAM Rev., 42 (2000), 451-484.
[17] L.L. Thompson, P. M. Pinsky, A Galerkin least squares finite element method for the two-dimensional Helmholtz equation, Int. J. Numer. Meth. Engng., 38 (1995), 371-397.
[18] L.P. Franca, E.G. Dutra do Carmo, The Galerkin gradient least-squares method, Comput. Methods Appl. Mech. Engrg., 74 (1989), 41-54.
[19] L.P. Franca, C. Farhat, A.P. Macedo, M. Lesoinne, Residual-free bubbles for the Helmholtz equation, Int. J. Numer. Meth. Engng., 40 (1997), 4003-4009.
[20] A.A. Oberai, P.M. Pinsky, A multiscale finite element method for the Helmholtz equation, Comput. Methods Appl. Mech. Engrg., 154 (1998), 281-297.
[21] C. Farhat, I. Harari, L.P. Franca, The discontinuous enrichment method, Comput. Methods Appl. Mech. Engrg., 190 (2001), 6455-6479.
[22] R. Tezaur, I. Kalashnikova, C. Farhat, The discontinuous enrichment method for medium-

https://doi.org/10.4208/cicp.110415.240316a Published online by Cambridge University Press

frequency Helmholtz problems with a spatially variable wavenumber, Comput. Methods Appl. Mech. Engrg., 268 (2014), 126-140.
[23] D.J. Min, H. Yoo, C. Shin, H.J. Hyun, J.H. Suh, Weighted-averaging finite-element method for scalar wave equation in the frequency domain, J. Seism. Explor., 11 (2002), 197-222.
[24] M.N. Guddati, B. Yue, Modified integration rules for reducing dispersion error in finite element methods, Comput. Methods Appl. Mech. Engrg., 193 (2004), 275-287.
[25] G. Gabard, Discontinuous Galerkin methods with plane waves for the displacement-based acoustic equation, Int. J. Numer. Meth. Engng., 66 (2006), 549-569.
[26] M. Grigoroscuta-Strugaru, M. Amara, H. Calandra, R. Djellouli, A modified discontinuous Galerkin method for solving efficiently Helmholtz problems, Commun. Comput. Phys., 11 (2012), 335-350,
[27] I. Babuska, J.M. Melenk, The partition of unity finite element method: Basic theory and applications, Comput. Methods Appl. Mech. Engrg., 139 (1996), 289-314.
[28] T. Strouboulis, R. Hidajat, Partition of unity method for Helmholtz equation: q-convergence for plane-wave and wave-band local bases, Appl. Meth., 2 (2006), 181-204.
[29] L.Y. Yao, D.J. Yu, X.Y. Cui, J.W. Zhou, A hybrid finite element-least square point interpolation method for solving acoustic problems, Noise Control Eng. J., 60 (2012), 97-112.
[30] L.Y. Yao, J.W. Zhou, Z. Zhou, L. Li, Dispersion error reduction for acoustic problems using the finite element-least square point interpolation method, J. Vib. Acoust., 137 (2015), 021013.
[31] Ph. Bouillard, S. Suleau, Element-free Galerkin solutions for Helmholtz problems: Formulation and numerical assessment of the pollution effect, Comput. Methods Appl. Mech. Engrg., 162 (1998), 317-335.
[32] C. Wenterodt, O.V. Estorff, Dispersion analysis of the meshfree radial point interpolation method for the Helmholtz equation, Int. J. Numer. Meth. Engng., 77 (2009), 1670-1689.
[33] X.Y. Cui, P.W. Liu, G.Y. Li, An element decomposition method with variance strain stabilization, Sci. China-Phys. Mech. Astron., 58 (2015), 074601.
[34] F. Ihlenburg, I. Babuska, Reliability of finite element methods for the numerical computation of waves, Adv. Eng. Softw., 28 (1997), 417-424.
[35] I. Harari, C.L. Nogueira, Reducing dispersion of linear triangular elements for the Helmholtz equation. J. Eng. Mech., 128 (2002), 351-358.

https://doi.org/10.4208/cicp.110415.240316a Published online by Cambridge University Press